Open Access Earth System Science Data Discussions

A 250m annual alpine grassland AGB dataset over the Qinghai-Tibetan Plateau (2000-2019) based on in-situ measurements, UAV images, and MODIS Data

Huifang Zhang [1,2,3], Zhonggang Tang[2], Binyao Wang [2], Hongcheng Kan [2] ,Yi Sun[1,2], Yu Qin[3], Baoping
5 Meng[1,2], Meng Li[1,2], Jianjun Chen[4], Yanyan Lv[1,2], Jianguo Zhang[1,2] Shuli Niu[5], Shuhua Yi [1,2,]*

[1]Institute of Fragile Eco-environment, Nantong University, 999 Tongjing Road, Nantong, Jiangsu, 226007, China
[2]School of Geographic Science, Nantong University, 999 Tongjing Road, Nantong, Jiangsu, 226007, China
[3]State Key Laboratory of Cryospheric Sciences, Northwest Institute of Eco-Environment and Resources, Chinese Academy
10 of Sciences, 320 Donggang West Road, Lanzhou 730000, China
[4]College of Geomatics and Geoinformation, Guilin University of Technology, 12 Jiangan Road, Guilin 541004, China;
[5]Key Laboratory of Ecosystem Network Observation and Modeling, Institute of Geographic Sciences and Natural Resources
Research, Chinese Academy of Sciences, Beijing, China

15 *Correspondence to:* Shuhua Yi (yis@ntu.edu.cn)

Abstract. The alpine grassland ecosystem accounts for 53% of the Qinghai-Tibet Plateau (QTP) area, which is an important ecological protection barrier, but fragile and highly vulnerable to climate change. Therefore, continuous monitoring of the aboveground biomass (AGB) of grassland is necessary. Although many studies have mapped the spatial distribution of AGB over the QTP, the results vary widely due to the limited ground samples and mismatches with satellite pixel scales. This
20 paper proposed a new algorithm using unmanned aerial vehicles (UAVs) as a bridge to re-estimate the grassland AGB over the QTP from 2000 to 2019. The innovations were as follows: 1) In the aspect of ground data collection, the spatial scale matching among the traditional ground quadrat sampling, UAV photos, and MODIS pixels was fully considered. From 2015 to 2019, 906 pairs of ground-UAV sample data at the quadrat scale and 2,602 sets of UAV data matching the MODIS pixel scale were collected. A total of more than 37,000 UAV photos were captured at the height of 20 meters. Therefore, the
25 ground validation samples was sufficient and scale matched. 2) In terms of model construction, the traditional quadrat scale (0.25m²) was successfully upscaled to the MODIS pixel scale (6,2500 m²) based on the random forest method and stepwise upscaling scheme. Compared with previous studies, the scale matching of independent and dependent variables was realized, effectively reducing the impact of scale mismatch. At the pixel scale, the AGB value estimated by UAV had a more linear correlation with the MODIS vegetation indices than the traditional sampling method. The multi-year independent cross-
30 validation results showed that the constructed pixel scale AGB estimation had good robustness, with an average R^2 of 0.83 and RMSE of 34.13 g/m². Our dataset provides an important input parameter for a comprehensive understanding of the QTP in the process of global climate change. The dataset is available from the National Tibetan Plateau/Third Pole Environment Data Center (https://doi.org/10.11888/Terre.tpdc.272587, Zhang et al., 2022).

Open Access Earth System Science Data Discussions

1 Introduction

35 Grasslands, accounting for approximately 37% of the earth's surface, play an essential role in global carbon cycling and food supply (O'mara, 2012). However, most natural grasslands have been degraded to a certain extent due to overgrazing, farmland encroachment, soil erosion, and global climate change (Suttie et al., 2005; Ramankutty et al., 2008; O'mara, 2012). Therefore, timely monitoring of grassland health is crucial for sustainable development and understanding the global carbon cycling processing. Aboveground biomass (AGB) is a key indicator of grassland status and an important input parameter of

40 the ecological model and carbon storage estimation. Thus, accurate and rapid estimation of AGB is valuable for grassland monitoring.

The advent of satellites makes it possible to map the spatial distribution and temporal dynamics of grassland over large areas. Spectral information from different satellites has been employed for biomass estimation, such as Sentinel-2, Landsat, and

45 MODIS (Wang et al., 2019; Zhang et al., 2016). Although there are differences in spatial and spectral resolution, the core idea of building a biomass model is constructing the linear or nonlinear relationships between the field measured samples and various satellite spectral indices. Therefore, the estimation accuracy is closely related to the quality and quantity of ground samples (Morais et al., 2021; Yu et al., 2021). There are still two deficiencies in ground data collection: the large spatial scale gap between the traditional samples and satellite pixels, and the low efficiency.

50

How to narrow the spatial gap between traditional samples and satellite pixels is an urgent problem to be solved. Since it is impossible to harvest all the grass within a pixel range, an average of 3-5 quadrat size samples (0.5 m × 0.5 m or 1m × 1m) is usually used as the measurement (Dusseux et al., 2015; Yang et al., 2017), which results in a considerable spatial gap. A lot of studies have been carried out to upscale ground measurements to satellite pixels (Crow et al., 2012; Bian and Walsh,

55 1993), such as block Kriging geostatistical interpolation, different types of regression models, or machine learning algorithms (Cheng et al., 2007; Wang et al., 2014; Cannavacciuolo et al., 1998; Dancy et al., 1986; Li et al., 2018). However, the accuracy of these methods depends on the density of sampling points. In addition, fine-resolution satellites were used as a bridge to reduce the impact of scale mismatch on AGB estimation (Yu et al., 2021; He et al., 2019). The primary reason is that the spatial gap between traditional ground data and fine-resolution satellites is much smaller than medium or coarse-

60 resolution satellites (Wang and Sun, 2014). Therefore, obtaining a value matching the pixel scale is the key to improving the AGB inversion accuracy from remote sensing.

Improving the efficiency of ground sampling is the other problem to be solved. Although the traditional field sampling method can get high accuracy results, it is time-consuming and labor-intensive. Large-region grassland AGB inversion often

65 requires years of accumulation to obtain ground observation samples with sufficient spatial representation. For example, it took Yang et al. five years to complete the collection of ground samples to investigate the grassland AGB in China (Yang et

al., 2010). Moreover, some scholars had expanded the sample size by using the data published by others when the original ground data was limited (Xia et al., 2018; Jiao et al., 2016). Considering the differences in the plot area, quadrat size, and sampling method, datasets from different sources may affect the overall inversion accuracy.

70

The development and popularization of unmanned aerial vehicle (UAV) technology provides new ideas for solving the above problems. UAV images have been successfully used to estimate ecological indicators such as FVC, biomass, and canopy height (Chen et al., 2016; Zhang et al., 2018; Bendig et al., 2015). Compared with traditional sampling methods, the use of UAVs has the following incomparable advantages. First, UAVs can effectively obtain 2D or 3D information about vegetation structure without destroying it, which is helpful for the estimation of grassland biomass (Lussem et al., 2019; Zhang et al., 2022; Zhang et al., 2018). Second, UAVs can easily collect key parameters of grassland within satellite pixels (e.g., FVC, Chen et al. 2016). Hence, UAV images can be used as a bridge to reduce the spatial gap between the field sampling and the satellite pixel. However, most UAV-based grassland biomass estimations are small-scale, with few regional-scale studies. It is still unknown whether UAVs can be used to narrow the spatial gap between the traditional ground samples and satellite pixels. In addition, due to the limited sample size, previous regional-scale grassland AGB models lacked independent years of cross-validation to test the robustness of the model in different periods.

This study proposed a new method combining traditional ground sampling, UAV photographing, and satellite data to generate a new reliable AGB dataset of QTP. The objectives of this study were: 1) to construct the UAV-based grassland AGB estimation models at quadrat/satellite pixel scales, respectively; 2) to investigate whether UAVs can be used as a bridge to narrow the spatial gap between traditional ground observation samples and satellite pixels, and improve the estimation accuracy of grassland AGB; 3) to map the AGB of alpine grassland on the Qinghai-Tibetan Plateau (QTP) during the 2000~2019.

2 Materials and Methods

2.1 Study Site

QTP is the highest and largest plateau on the earth (26°00′12″~39°46′50″N, 73°18′52″~104°46′59″E) with an average elevation of ~4000 m and an area of approximately 257.24×10^4 km^2 (Figure 1). It is located in western China, and the annual average temperature and precipitation are around 1.6°C and 413.6 mm, respectively. The main grassland types are alpine meadows, alpine steppe, and sparse grassland, which play a critical role in climate regulation, water conservation, and biodiversity protection (Ding et al., 2013). However, grassland ecosystems are fragile and vulnerable to global climate change and human activities, and have high spatial heterogeneity.
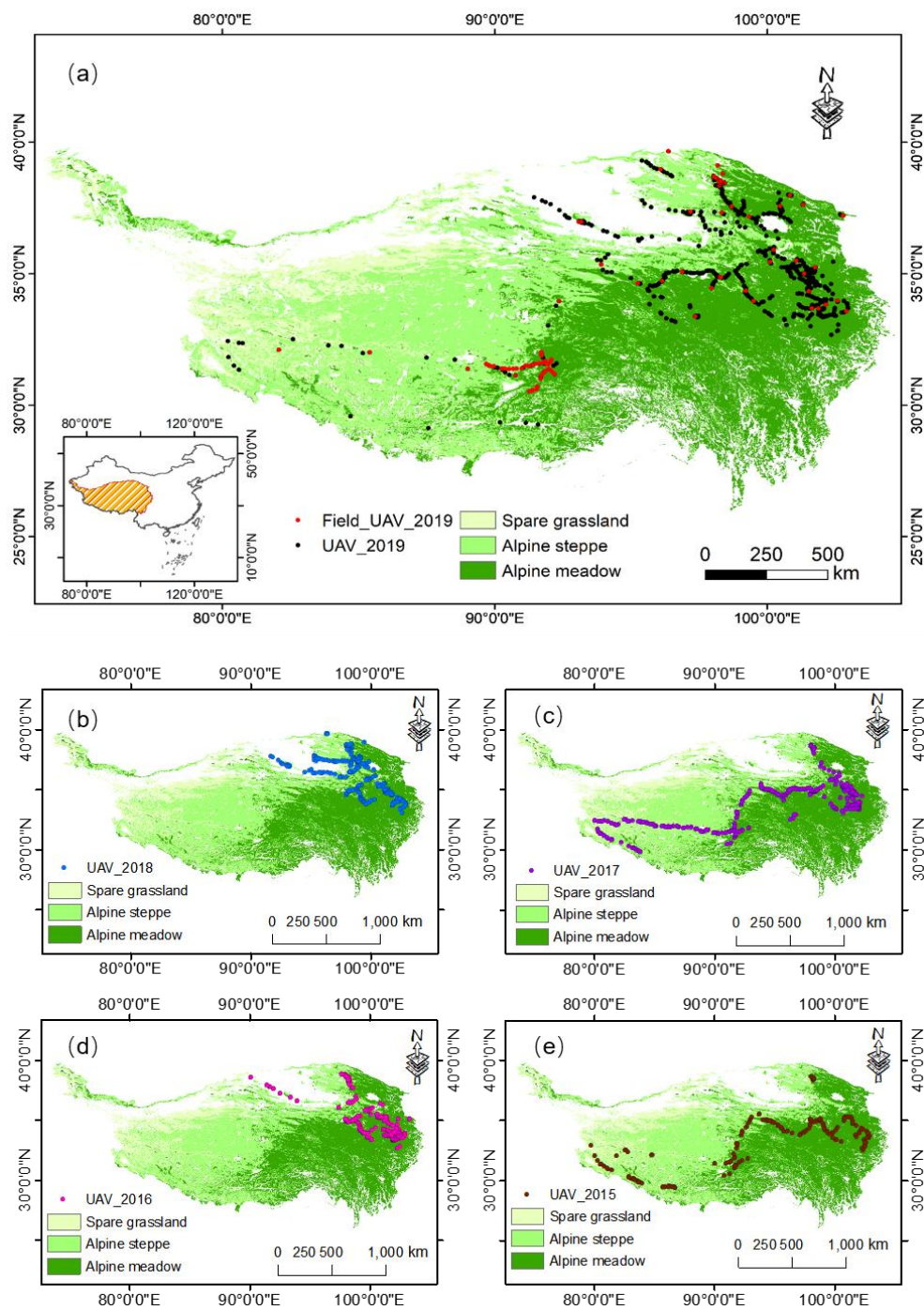
Figure 1. Distribution of field and UAV sampling sites of 2019 (a); and UAV sampling sites of 2015-2018 in alpine grasslands on the QTP (b-e). Field_UAV_2019 represents quadrat scale sampling sites for the 2019 UAV-Field synchronous grassland biomass experiment. UAV_year represents the UAV sampling point based on the GRID or RECTANGE flight mode of the corresponding year.

2.2 Overall technology roadmap

The overall flowchart of UAV-field investigation and the construction of grassland AGB estimation model at different
105   spatial scales were shown in Figure 2, which mainly includes four steps: 1) UAV and field investigation; 2) constructing the
grassland AGB estimation model at the quadrat scale; 3) upscaling the AGB to the MODIS pixels; 4) building the final AGB
estimation model at MODIS pixel scale and applying it to the QTP region. More detailed information about each step was
described in the following sections.
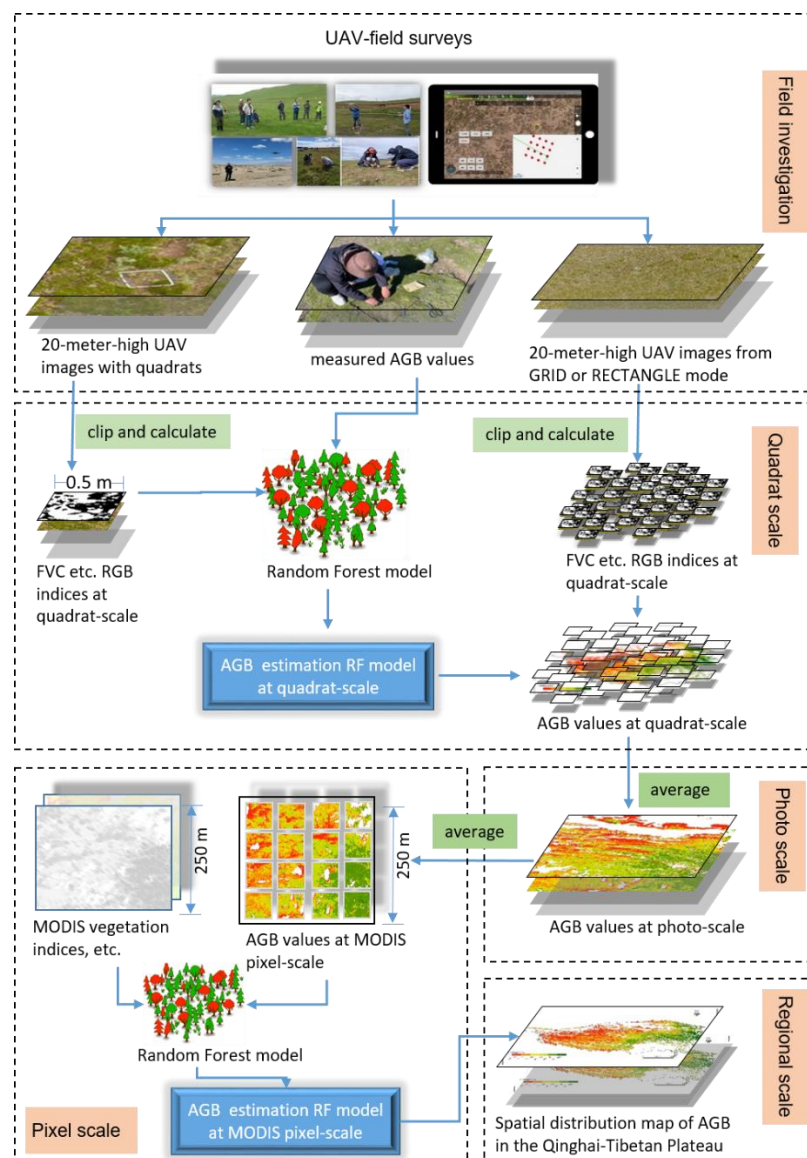
110

**Figure 2. The overall flowchart of UAV-field investigation and the construction of grassland AGB estimation models at different
spatial scales.**

2.3 Field investigation

2.3.1 UAV and route planning

115 DJI Phantom 3 professional (DJI Company, Shenzhen, China), a popular consumer quadrotor UAV equipped with a high-resolution RGB camera, was used to collect UAV images of the QTP from 2015 to 2019. It has a 1/23-inch CMOS sensor and is capable of taking 12-megapixel photos. In addition, it uses a 3-axis stable gimbal to take photos downward vertically and eliminate the distortion of UAV images. It has good environmental adaptability, the working temperature ranges from 0° to 40°, and the highest take-off altitude can reach 6000 meters. Therefore, it can adapt well to the low temperature and high 120 altitude of the QTP. More detailed information about the UAV system is listed in Table A1.

Fragmentation Monitoring and Analysis with aerial Photography (FragMap) system, which can realize long-term collaborative observation, was used for UAV route planning (Yi, 2017). The repeatability of UAV observation is the basis for understanding the ecological process. Through FragMap, we conducted UAV observations on the QTP from 2015 to 125 2019 (Figure 1). Over 2,000 fixed flight routes were set during this period, and more than 37,000 UAV images were collected, providing a reliable UAV data set for this study (Table 1).

**Table 1. UAV sampling information from 2015 to 2019**

Year	Flight Mode	Number of routes	Photo number	Acquisition time
2015	RECTANGLE	214	2568	7.05 ~8.24
2016	RECTANGLE	334	4008	6.20~9.29
	GRID	150	2400	6.20~9.23
2017	RECTANGLE	315	3780	5.10~10.24
	GRID	322	5152	7.15~8.22
2018	RECTANGLE	79	948	7.22~8.03
	GRID	303	4848	7.04~8.29
2019	GRID	885	14160	7.12~9.21
	Total	**2602**	**37864**	

130

GRID, RECTANGLE, and BELT are the most commonly used flight modes in the FragMap software. The GRID and RECTANGLE modes have 16 and 12 waypoints for capturing UAV images within a MODIS pixel range (Figure A1). Their flying height and speed are set to 20 m and 3m/s, respectively. The BELT mode is similar to GRID but is designed to get near-ground UAV image data with a higher resolution (Figure 3b). It can be combined with the traditional sampling method

135   to ensure that UAV images are consistent with the ground quadrats (Figure 3d). Generally, the BELT size is set to 40 m × 40 m, and the flying height and speed are set to 2 m and 1 m/s to ensure that field workers have enough time to place a sampling quadrat on the UAV shooting waypoint. As with GRID mode, 16 UAV images can be captured during one flight.
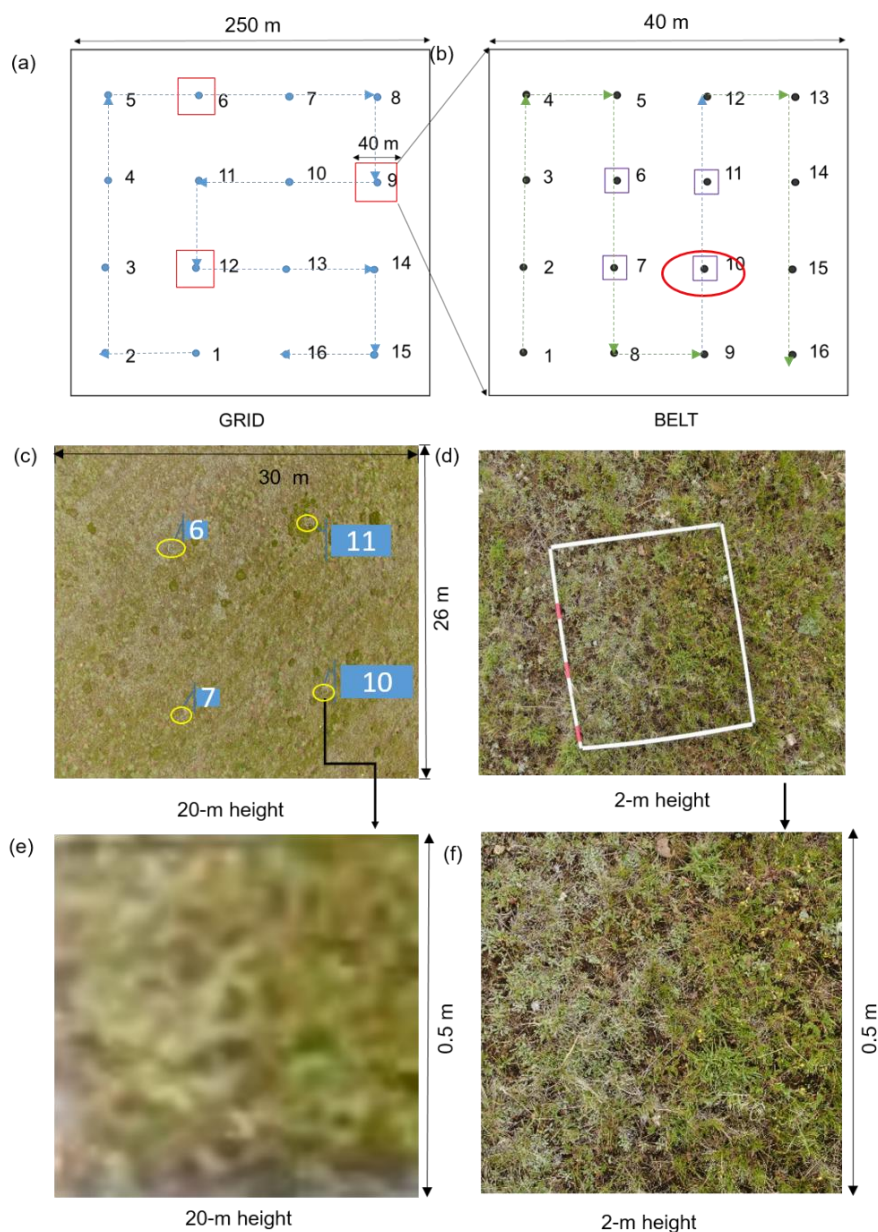
140   **Figure 3. Schematic diagram of the UAV-field synchronization experiment in 2019: a combination design of GRID (a) and BELT (b) flight modes; a UAV image with a quadrat from the BELT mode at the height of 2 m (d); a 20-meter-high UAV image including four sample quadrats (c); and the cropped UAV images at quadrat scale from 20 m (e) and 2 m (f) height, respectively.**

2.3.2 Synchronization experiment of UAV and field sampling

A UAV-field biomass synchronization experiment was designed in 2019 to ensure spatial matching among satellites, UAVs,
145 and ground sampling (Figure 3). The specific implementation steps were as follows. First, we set a GRID flight mode with
the MODIS pixel size (250 m × 250 m) (Figure 3a). Then, three waypoints from the GRID route were randomly selected for
setting the BELT routes (40 m × 40 m). For each BELT, we placed a sampling quadrat (0.5 m × 0.5 m) at its 6, 7, 10, and 11
waypoints to ensure that the GRID image can contain the four quadrats described above (Figure 3b-c). Grassland AGB
samples were then cut, bagged, and numbered at the end of all flights. Finally, these samples were oven-dried at 65℃ to
150 constant weight to obtain the field-measured AGB values.

2.4 Data processing

2.4.1 UAV photo preprocessing and indices calculation

UAV photo preprocessing included image quality inspection, image cropping, and calculation of different indices. First, we
155 eliminated the overexposed or blurry 20-meter-high UAV images. Second, the pixels in the sampling quadrat were cropped
and saved (Figure 3e). Third, we calculated the RGB indices for the cropped UAV images. Similar to our previous study,
indices included color space, histogram, and vegetation indices, details of which could be found in reference (Zhang et al.,
2022). In addition, 30 other RGB vegetation indices were added as candidate independent variables. The names, formulas,
and references of the above indices were shown in Table A2.

2.4.2 MODIS vegetation index and other spatial data

The MOD13Q1(v006) product was downloaded from the NASA earth explorer website (https://earthexplorer.usgs.gov/) for
the inversion of the alpine grassland AGB on the QTP. The data contained two commonly used vegetation indices,
normalized vegetation index (NDVI) and enhanced vegetation index (EVI), with spatial and temporal resolutions of 250 m
and 16 days, respectively. A total of 2,842 scenes from 2000 to 2019 were downloaded. Then, the MODIS images were
165 reprojected and stitched using the MODIS projection tool (MRT). After that, we used the point extraction function in
ArcGIS software to get the corresponding vegetation indices of the UAV samples to construct the pixel-scale AGB
estimation model. In addition, based on the NDVI index and the formula kNDVI= TANH (NDVI^2), the kNDVI index was
calculated to overcome the NDVI saturation issue (Camps-Valls et al., 2021). The annual maximum vegetation indices were
calculated by the maximum value composition (MVC) algorithm of ENVI software to estimate the spatial AGB distribution
170 of QTP from 2000 to 2019.

Furthermore, the meteorological, soil texture, and topographic data were also included as candidate independent variables for
constructing the pixel-scale AGB estimation model. Meteorological factors, including the annual mean temperature (TA),

annual mean precipitation (PREC), and annual total solar radiation (RAD), were calculated based on the daily
meteorological dataset from the National Meteorological Information Center of China. The data processing steps mainly
included interpolation, cumulative summation, and annual averaging processing to obtain the meteorological raster dataset
with a spatial resolution of 1000 meters (Li et al., 2021). Moreover, the spatial distribution data of soil texture with 1 km
spatial resolution, including the ratio of soil organic matter (SOM), clay, sand, and silt, were downloaded from the Resource
and Science and Data Center of China (https://www.resdc.cn/). All the meteorological and soil datasets were resampled into
250 m by ArcGIS software to match the MODIS data.

Terrain factors include the digital elevation model (DEM), slope, and aspect. The DEM was from shuttle radar topography
mission (SRTM) images (version 004, 90 m) and resampled to 250 m. Slope and aspect were then calculated from the DEM
data using the terrain analysis tools of ArcGIS software.

2.5 AGB modeling and computation at different scales

We estimated the grassland AGB at three scales: the quadrat scale, photo scale, and satellite pixel scale (Figure 4). More
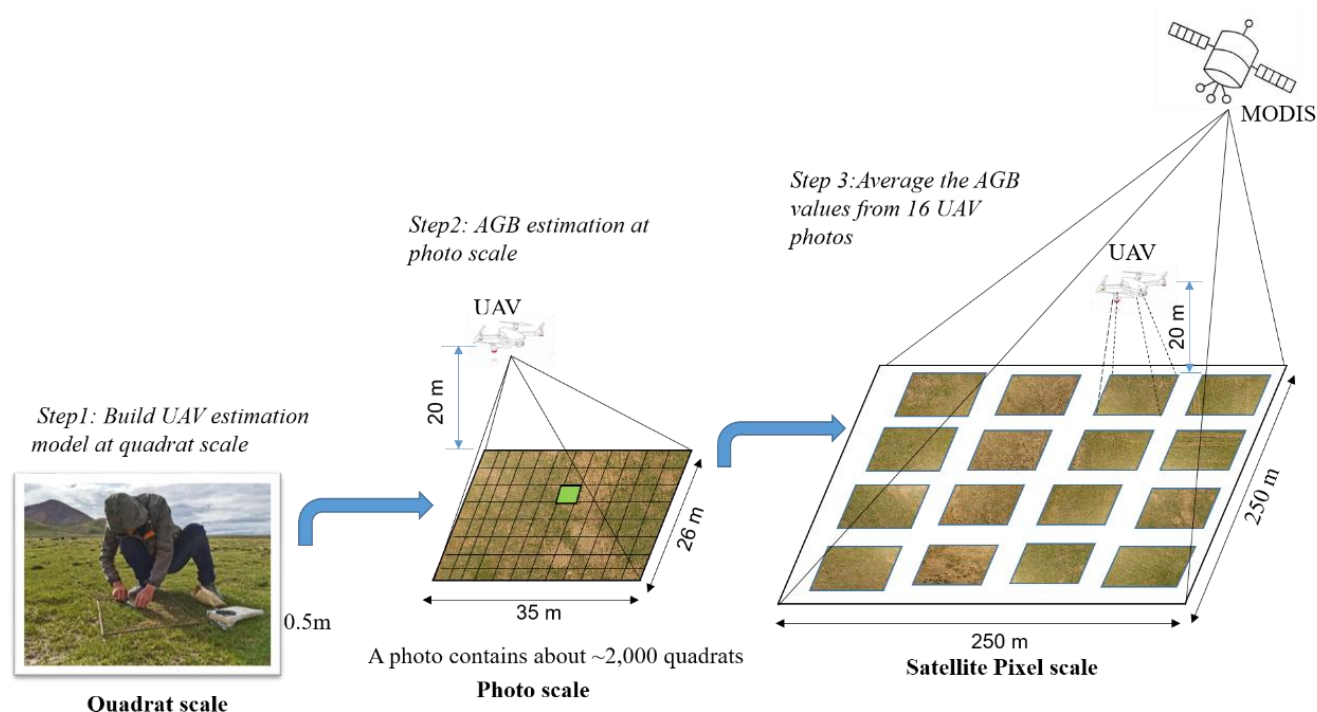detailed information was described as follows.

Figure 4. Upscaling steps to estimate grassland AGB matching the MODIS pixel scale.

2.5.1 Modeling method

Random Forest (RF) (Breiman, 2001), an ensemble-learning algorithm, was employed to estimate AGB at different scales due to its excellent performance in biomass estimation (Ghosh and Behera, 2018; Mutanga et al., 2012; Wang et al., 2016). Two main parameters, the number of regression trees in the forest (*ntree*) and the number of feature variables required to create branches (*mtry*), were optimized based on the root mean square error (RMSE) of training data at first. Here, the *ntree* values were tested from 100 to 5000 with an interval of 100, and the *mtry* was set as the square root of the number of training sample features. In addition, the importance of each predictor was ranked by calculating the percentage increase in mean square error (%IncMSE).

The backward feature elimination method (BFE) was used to reduce the number of input variables to simply the RF model (Vergara and Estévez, 2014). The main steps were as follows: 1) constructing an AGB RF model by including all predictor variables in the initial stages and calculating the %IncMSE index for each variable; 2) eliminating the least promising variable and then rerunning the RF model until only one independent variable was left. Moreover, the corresponding coefficient of determination (R^2) and the corresponding root mean square error (RMSE) were calculated in each iteration；3) selecting the smallest subset of variables with the highest R^2 as the final optimized indices.

In addition, different training and validation strategies were used at different scales. At the quadrat scale, a 10-fold cross-validation method was used due to the limited ground samples (Kohavi, 1995). At the pixel scale, 30% of the UAV-estimated AGB samples in 2019 were randomly selected as an independent validation dataset due to the large sample size. Meanwhile, cross-year validation was performed using UAV-estimated AGB values from 2015 to 2018 to test the robustness of the model over different periods.

### 2.5.2 AGB RF estimation model at the quadrat scale (0.25 m²)

A total of 906 pairs of quadrat-scale UAV-field AGB observation data were collected, with good spatial representativeness (Figure 1 a, red dots). The observed AGB values ranged from 0 g/m² to 450 g/m², with mean and median values of 59.75 g/m² and 33.04 g/m², respectively, most of which were less than 100 g/m² (Figure 5a). Then, the cropped 20-meter-high UAV image indices and the measured AGB values were used as the independent and dependent variables to build the RF model (Figure 2).

2.5.3 AGB calculation at the photo scale (~900 m²)

The steps for AGB estimation of the entire 20-meter-high UAV photo were as follows: 1) First, each UAV photo was divided into ~2,000 quadrat-sized small patches. 2) Second, the AGB of each small patch was calculated based on the quadrat-scale AGB estimation model. 3) Finally, the average value of all the small patches was calculated as the AGB of the

whole photo. Based on the above steps, the AGB values of 37,487 images in GRID or Rectangle mode were calculated using over 74 million AGB values at the quadrat scale (Table 1).
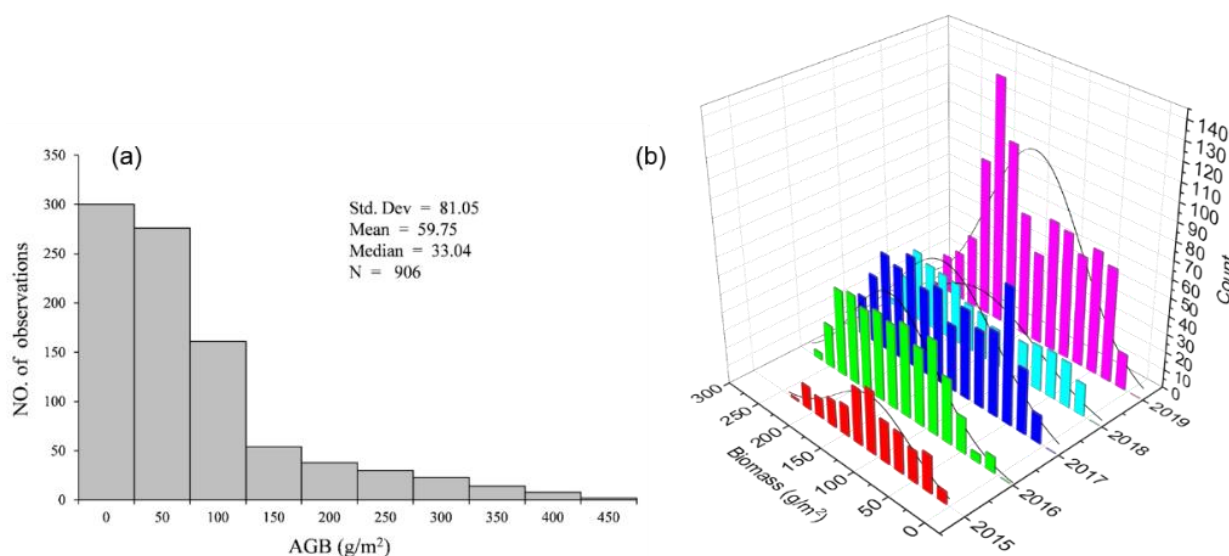
225 **Figure 5. Histograms of field-measured AGB values at quadrat scale (a) and UAV-estimated AGB values of different years at the photo scale (b).**

2.5.4 AGB RF model construction at MODIS pixel-scale (6,2500 m^2)

The following steps were involved in constructing the AGB estimation model at the pixel scale. 1) Since the coverage of a
230 GRID or RECTANGLE route was similar to that of the MODIS pixel, the average of its 16 or 12 photos was taken as the AGB value of the corresponding pixel. 2,602 UAV-estimated AGB samples were obtained at the pixel scale from 2015 to 2019 (Table 1). 2) The MODIS vegetation indices and other spatial metrics corresponding to each GRID or RECTANGLE route were then extracted using the ArcGIS software. 3) Subsequently, the UAV-estimated AGB values and the extracted spatial indices were used as dependent and independent variables to build the AGB estimated model at the pixel scale using
235 the RF algorithm.

2.6 Uncertainty analysis

Since the actual AGB values of MODIS pixels cannot be directly obtained, vegetation indices were used to quantify the uncertainty of different AGB estimation methods. In other words, the higher correlation between the estimated AGB and MODIS vegetation indices, the higher accuracy of the estimation model was. This study firstly compared the correlation
240 between the MODIS vegetation indices and AGB values obtained by traditional sampling and UAV estimation methods. We

also explored the uncertainties of UAV sampling coverage by randomly combining the number of photos in a MODIS pixel, and tested whether the estimated AGB was closer to the true value as the number increased. Furthermore, the AGB validation results from GRID or RECTANGLE at the pixel scale were compared to understand the uncertainties caused by different flight modes.

3 Results

3.1 Independent variables selected for AGB modeling

The selected independent variables for AGB estimation at quadrat and pixel scales were listed in Table 2. A total of 36 independent variables were finally selected at the quadrat scale, including 26 vegetation RGB indices, 6 histogram indices, and 4 color space indices (Figure A2). At the pixel scale, five variables were selected, including NDVI, kNDVI, EVI, PREC, and DEM (Figure A3).

Table 2: Selected independent variables for the AGB modeling at quadrat and pixel scales. The full name of each variable at the quadrat scale was listed in Table A2.

Scale	Model	Number	Independent variables
Quadrat	RF_Q	36	FVC, WI, GI, EXG, TGI, EXGR,VEG, GRATIO, COM, CIVE, RGBVI, EXR, GLA, GRRI, MVARI, MGRVI, GRVI, RGRI, GBRI, VARI, NDI, RRATIO, EXB, V, IPCA, INT,
			HOC_R_CORR, HOC_B_CHIS, HOC_R_CHIS, HOC_G_CHIS, HOC_G_CORR, HOC_B_CORR
			B, H, G, R,
Pixel	RF_P	5	NDVI, kNDVI, EVI, DEM, PREC

3.2 Modeling and accuracy assessment

The estimated AGB values at the quadrat scale fitted well with the measured values (R^2 =0.73, RMSE=44.23 g/m^2), especially for the AGBs below 150 g/m^2 (Table 3, Figure 6a). However, there was an underestimation of high biomass (AGB > 200 g/m^2), probably due to the limited number of samples (Figure 5a).

Although the UAV sample size varied yearly, the estimated AGB values at the photo scale ranged from 0 to 300 g/m^2 (Figure 5b). The mean UAV AGB in 2016-2019 was around 150 g/m^2, while it was slightly lower in 2015 with 108 g/m^2. Cross-year validation results indicated that the constructed pixel scale AGB estimation model achieved good accuracy and robustness in different years (Figure 6b~f). The R^2 was 0.85 in 2017-2019 and slightly lower in 2015-2016 with 0.63 and

0.77, respectively (Table 3). There was a high correlation between the predictions and the UAV estimates, and the fitted line
265   was close to the 1:1 line (Figure 6 b~f).

Table 3: Calibration and validation results of AGB models at quadrat and pixel scales

Scale	Year	Training set		Validation set	
		R^2	RMSE(g/m^2)	R^2	RMSE(g/m^2)
Quadrat-scale	2019	0.94	20.18	0.73	44.23
Pixel-scale	2019	0.96	10.68	0.85	25.80
	2018	—	—	0.85	39.15
	2017	—	—	0.85	36.49
	2016	—	—	0.77	32.25
	2015	—	—	0.63	36.98

3.3 Correlation analysis between AGB values and MODIS indices

270   The correlations between the UAV-estimated AGB values and MODIS vegetation indices were much better than the
traditional ground sampling method (Figure 7a). For example, the correlation between NDVI and traditionally measured
AGB was only 0.53, much lower than that obtained from a single UAV image (r=0.74). Moreover, the correlation between
NDVI and UAV-estimated AGB increased with the number of UAV photos. It increased rapidly as the number increased
from 1 to 4 (from 0.74 to 0.86), then slowed down (from 0.87 to 0.88).

275

In addition, we compared the scatter plots and fitting lines between NDVI and different AGB estimation methods (Figure
7b-f). The results showed a weak linear relationship between the traditional measured AGB and NDVI, and the R^2 was only
0.29. Linearity was greatly improved using the UAV sampling method and increased with the number of photos. The fit
coefficient R^2 increased from 0.54 to 0.78, much higher than the traditional sampling method (Figure 7).
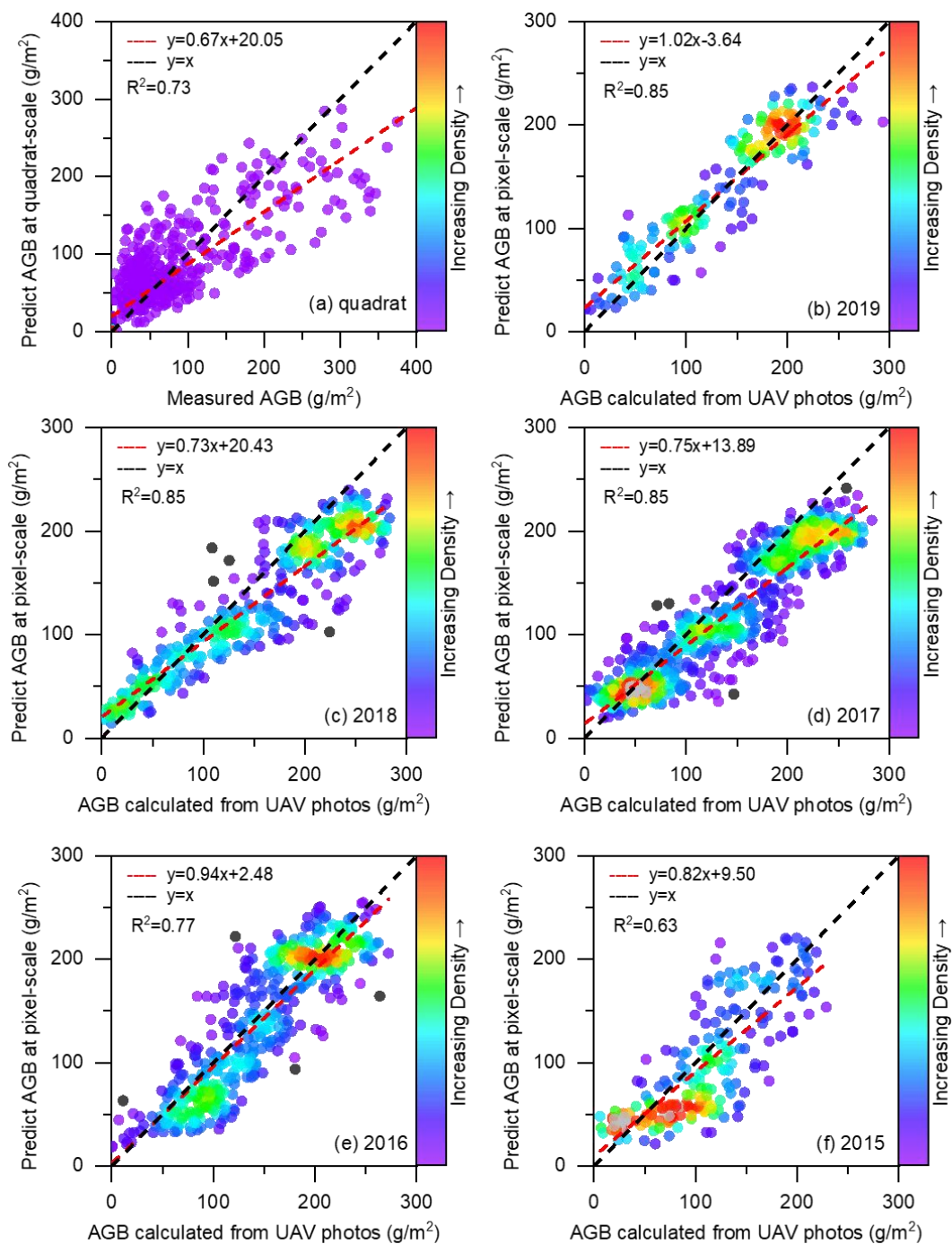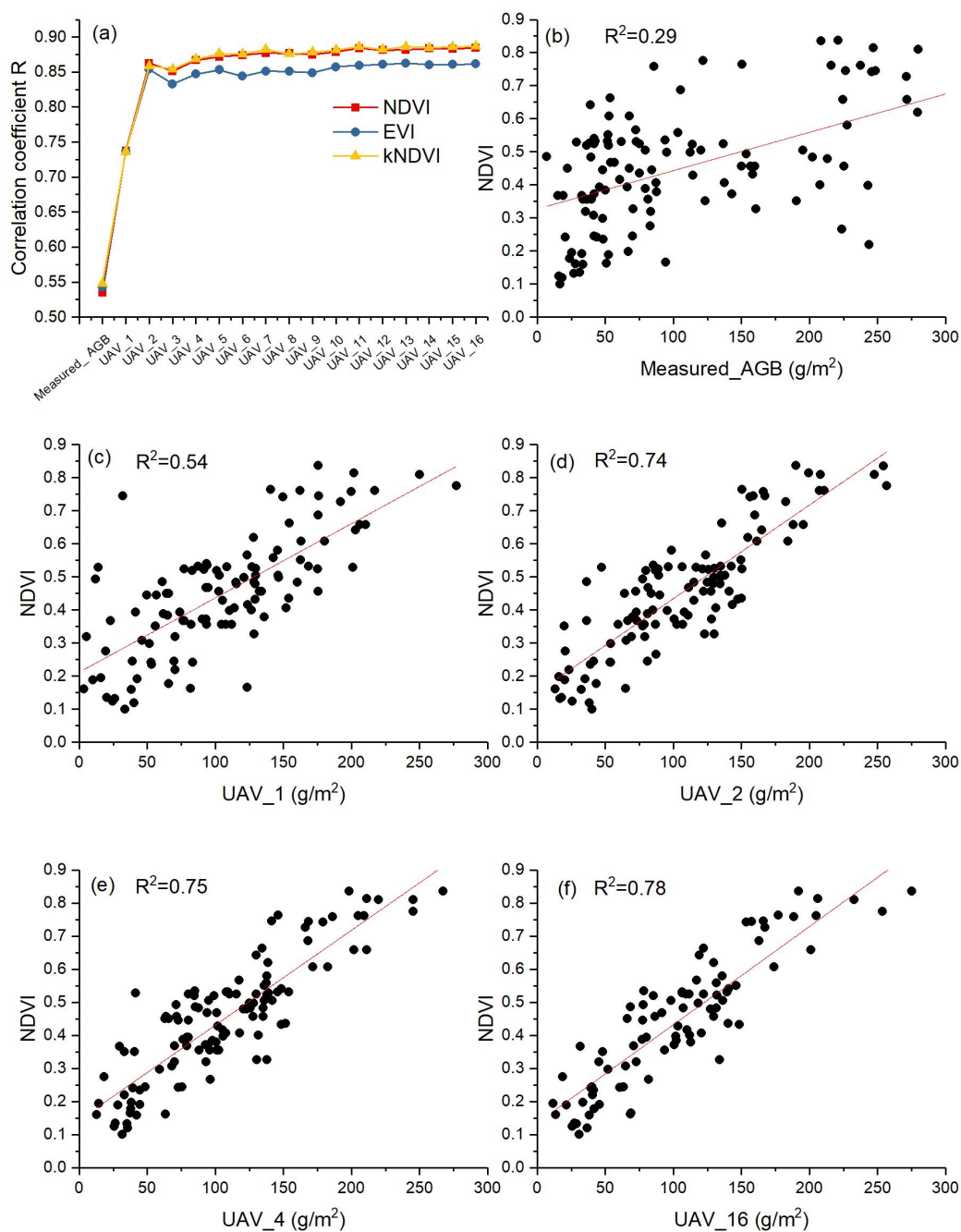
280

Figure 6. Validation results of the AGB estimation models at the quadrat (a) and MODIS pixel scale for 2015-2019 (b~f).

285

Figure 7. The correlations between the MODIS vegetation indices and different AGB estimation methods (a); the scatter plots between NDVI and different AGB estimation methods (b-f). UAV_x, x represents the number of UAV photos used to estimate the average AGB at MODIS pixel-scale. Here, the value range of x is from 1 to 16.

290

3.4 Spatial distribution of grassland AGB

The spatial distribution of the average grassland AGB on the QTP from 2000 to 2019 was calculated (Figure 8). The AGB gradually increased from west to east. From 2000 to 2019, the mean AGB on the QTP showed an insignificant increasing trend, with an average rate of 0.22 $gm^{-2}a^{-1}$ (Figure 9a). The overall mean AGB of the QTP was 103.6 g/m^2, and the mean

295 AGB of the alpine meadow, alpine steppe, and sparse grassland were 151.85 g/m^2, 60.85 $g/$, and 28.91 g/m^2, respectively (Figure 9b).
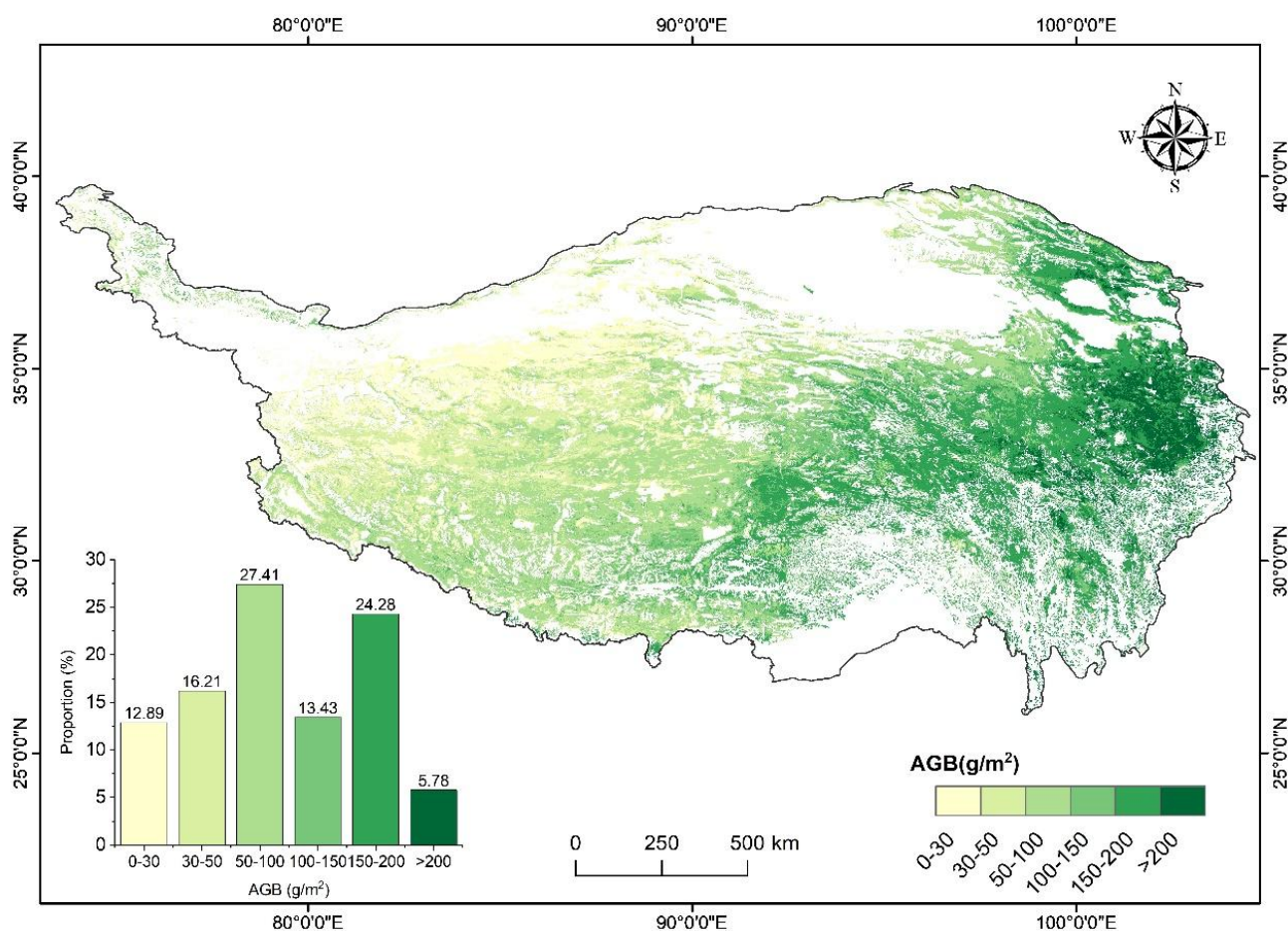
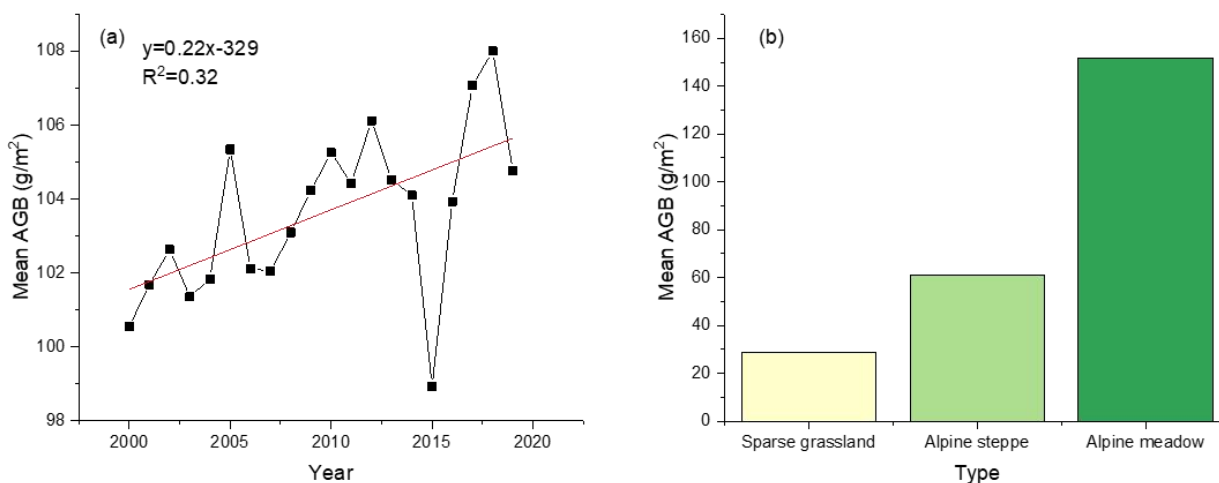300 **Figure 8. The spatial distribution of average grassland AGB on the Qinghai-Tibet Plateau during 2000-2019.**

16

Figure 9. Variation trend of average grassland AGB on the QTP from 2000 to 2019 (a) and average AGB of different grassland types (b).

4. Discussion

4.1 Scale matching and its influence factor

Unlike the previous studies (Yang et al., 2017; Yang et al., 2009; Meng et al., 2020), which directly represented the AGB value of a satellite pixel with the average value of 3-5 quadrat-scale samples, this study successfully upscaled the traditional quadrat scale to the MODIS pixel scale. We achieved the spatial scale matching of dependent and independent variables when calculating the AGB values at different scales. First, at the quadrat scale, the independent variables were all derived from cropped UAV images corresponding to the ground samples (Figure 3e). Then, the 20-meter-high UAV image was cropped into ~2000 quadrat-sized small patches to ensure consistency with the quadrat scale model, and the average of these patches was taken as the final AGB at the photo-scale. Finally, the AGB value that matched the MODIS pixel scale was calculated by the average value of 16 or 12 UAV photos within the MODIS pixel (Figure A1). Through the above three steps, we successfully upscaled the measured AGB from the traditional quadrat scale (0.5 m×0.5 m) to the photo scale (26 m×35 m) and MODIS pixel scale (250 m×250 m). Our results showed that, at the pixel scale, the correlation between UAV_estimated AGB values and MODIS vegetation indices was higher than that of the traditional sampling method (Figure 7).

Furthermore, we found that the spatial coverage of the UAV sampling had a particular influence on the effects of scale matching. Our results indicated that the closer the spatial coverage of the UAV sampling to the satellite pixel, the higher correlation with MODIS spectral indices (Figure 7a). The comparison of the validation results of different flight modes also confirmed this. At the pixel scale, we found that UAV AGB estimates from the GRID mode had a higher correlation with the

mode predictions than the RECTANGLE flight mode (Figure 10). The reason was that the GIRD mode could obtain 16 photos in the MODIS pixel at a time, while the RECTANGLE mode could only take 12 photos.

325   The above results confirmed that UAVs could serve as a bridge to effectively narrow the scale gap between traditional observations and satellite data.
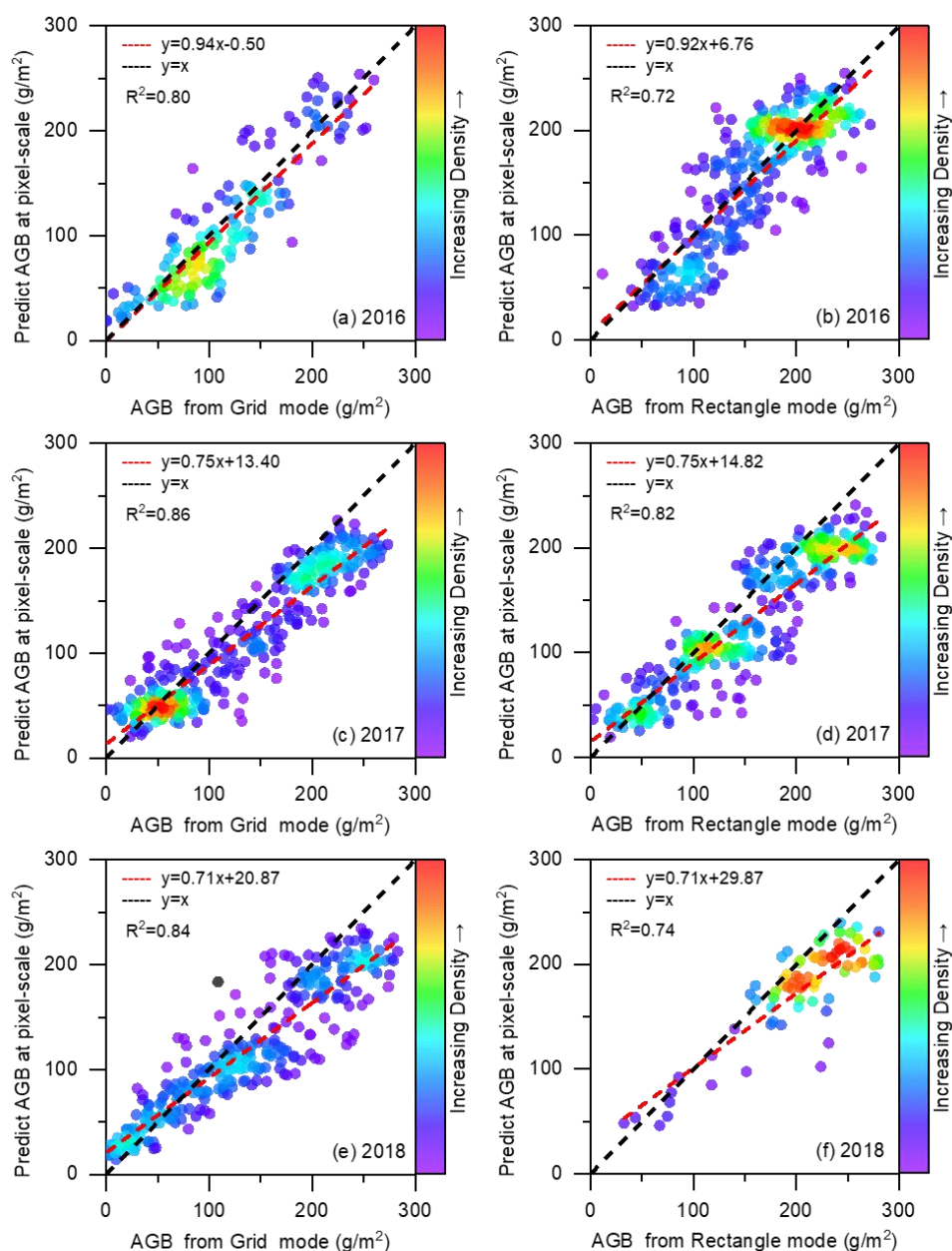

Figure 10. Comparison of validation results for the GRID (a,c,e) and RECTANGLE (b,d,f) modes in 2016-2018.

4.2 Importance of the addition of non-vegetation samples

330 Compared with traditional sampling, UAV sampling has the advantage of wide spatial coverage (0.5 m×0.5 m VS 35 m×26 m). Thus, vegetation and non-vegetation background information, such as roads, water, soil, gravel, riverbed, etc., were captured on the UAV photos (Figure 11). The addition of non-vegetated samples could improve the estimation accuracy of AGB at the photo scale, especially for low coverage areas, to avoid overestimation. The same was true for the pixel scale AGB estimation model. However, less consideration was given to the non-vegetated areas in the traditional method. The
335 sample plots were mainly set in areas with uniform spatial distribution but few in areas with spatial heterogeneity. This defect might limit the accuracy of AGB estimation due to the high spatial heterogeneity of the QTP. Fortunately, the UAV sampling method could avoid this drawback. It could objectively record the ground surface information with both vegetated and non-vegetated areas, resulting in a more objective AGB estimation at the pixel scale.
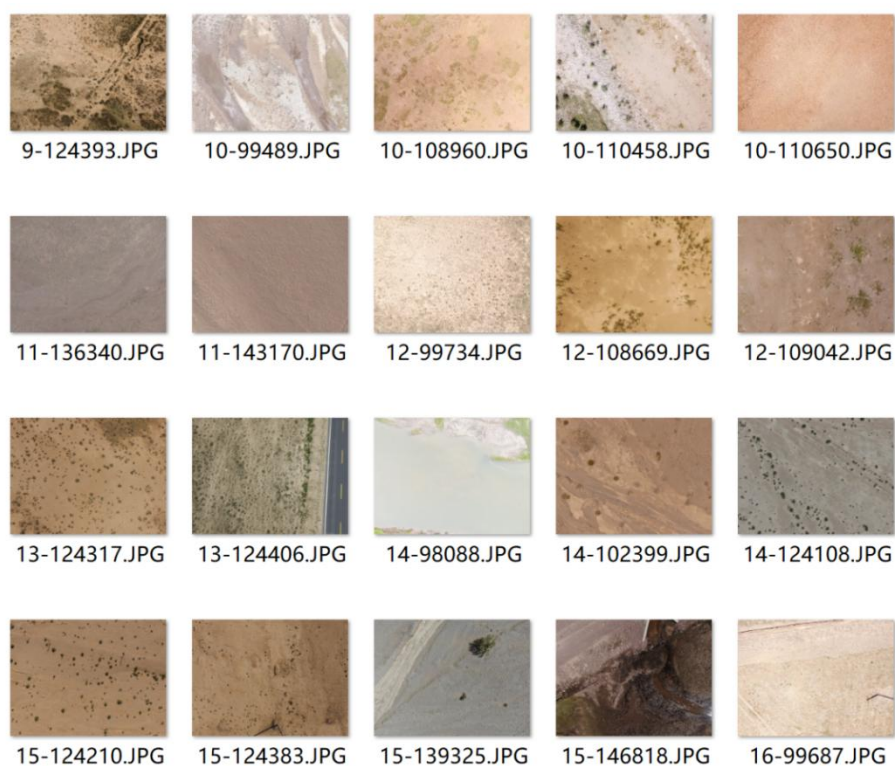
340

Figure 11. Examples of 20-meter-high UAV images with different non-vegetation background information.

19

4.3 Comparison of the estimated AGB with previous studies

345 In the following, the AGB estimation results of this study were compared with those of others at the quadrat scale, pixel scale, and regional scale.

At the quadrat scale, consistent with our previous study, we further confirmed that the UAV RGB images could be used to estimate grassland AGB at the quadrat scale over a large region (Zhang et al., 2022; Zhang et al., 2018). Similar to the 2-
350 meter-high UAV image, the indices from 20-meter-high UAV images could also be used to estimate the grassland AGB at quadrat-scale (R^2=0.73, RMSE=44.23 g/m^2). The quadrat-scale UAV model had an excellent grassland AGB estimation ability in the range of 0-150 g/m^2, and the verification points were mainly distributed near the 1:1 line (Figure 6a).

At the pixel scale, compared with other studies, this paper achieved the spatial scale matching of independent variables and
355 dependent variables in the modeling process (Yang et al., 2009; Yang et al., 2017). In addition, we implemented large-region and multi-year cross-validation in model verification. Despite differences in sample size and spatial distribution (Figure 1, Table 1), the validation results for 2017-2019 were similar (R^2=0.85). But in 2015-2016, R^2 was relatively low, at 0.63 and 0.77, respectively (Table 3, Figure 6). The reason was that during 2015-2016, due to the improper setting, many photos with abnormal white balance were obtained, which reduced the accuracy of the estimation (Figure 12). The validation results
360 indicated that the pixel scale AGB estimation model had good adaptability in different regions and periods while obtaining high-quality UAV images. Therefore, this method can be used to estimate the AGB values matching the satellite pixel scale in large regions.
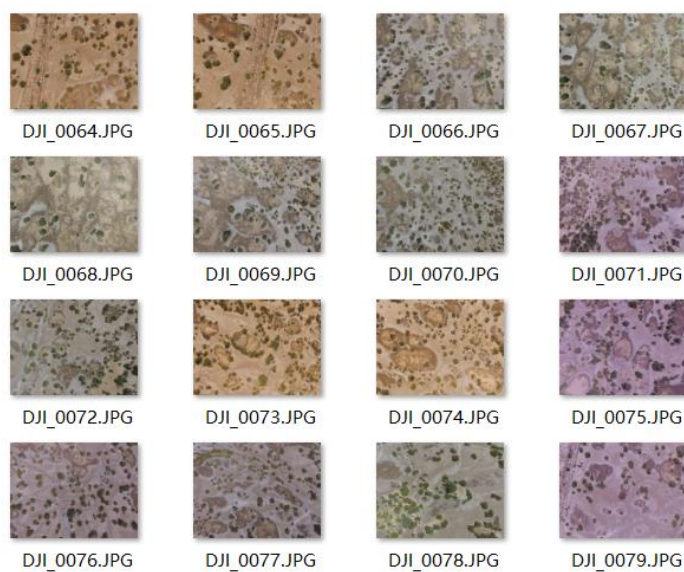

Figure 12. An example of a set of GIRD photos with abnormal white balance in 2015.

365

Table 4: Comparison of AGB estimation results of different studies on the QTP

Mean AGB (g/m²)	Alpine steppe (g/m²)	Alpine meadow (g/m²)	Study period	Approach	Data source	References
68.8	50.1	90.8	2001-2004	Linear regression	MODIS EVI	(Yang et al., 2009)
__	22.4	42.37	2000-2012	Linear regression	MODIS NDVI	(Liu et al., 2017)
78.4	__	__	1982-2010	RF	GIMMS	(Xia et al., 2018)
77.12	76.43	154.72	2000-2014	RF	MODIS	(Zeng et al., 2019)
59.63	42.75	77.56	2000-2017	RF	MODIS	(Gao et al., 2020)
120.73	__	__	1980–2014	regression	MODIS	(Jiao et al., 2016)
103.6	60.85	151.85	2000-2019	RF	MODIS	this study

At the regional scale, consistent with previous results, we found an overall increase in AGB over the QTP from 2001 to 2019, although there were fluctuations among years (Zeng et al., 2019; Gao et al., 2020). The annual mean AGB of grassland was

370   103.6 g/m², within the previously estimated range (59.63-120.73 g/m²) (Table 4). The mean AGB of different grassland types was different, among which the alpine meadow was 151.85 g/m², and the alpine steppe was 60.85 g/m². Our estimation results were similar to Zeng et al. (Zeng et al., 2019), but the overall average AGB was higher than their estimated 77.12 g/m². The difference between our estimated grassland AGB and previous studies might be due to differences in data sources and modeling methods. Unlike previous studies, we collected ground verification data by combining the traditional sampling

375   method and UAVs. The newly proposed method could overcome the shortcomings of traditional samplings, such as the time-consuming and labor-intensive. It no longer took years of work to obtain sufficient spatially representative ground verification data in large regions(Yang et al., 2017). Through UAV sampling, only 15~20 minutes were needed to complete a ground survey in a pixel range of 250 m × 250 m. In addition, it could effectively reduce the spatial gap between ground verification samples and satellite pixels.

380

Meanwhile, different modeling approaches might also affect the simulation results. Yang et al. found that the model performance of ANN was much better than the linear regression model when using the same dataset to estimate grassland AGB in the Three-River Headwaters Region of China (Yang et al., 2017). Jia et al. reported that the model forms could bring 13% uncertainty to the AGB estimation(Jia et al., 2016). Wang et al. compared the RF with the support vector regression

385   (SVR) machine learning algorithm and found that the RF yielded the best performance in grassland biomass estimation (Wang et al., 2017).

4.4 Limitations and further work

We acknowledge that there are some shortcomings in this study. 1) The sample size greater than 200 g/m^2 was insufficient at
390   the quadrat scale, leading to underestimation where AGB was high. We will enlarge the sample size to improve the
simulation accuracy in future research. 2) Although the grassland height information could help improve the estimation
accuracy of grassland AGB, it was still challenging to obtain grassland height information from UAV RGB images in a large
area. (Zhang et al., 2022; Lussem et al., 2019; Viljanen et al., 2018). Thus, in the next step, we will consider using the
affordable DJI Zensil L1 Lidar UAV to obtain grassland height information to improve the AGB estimation capability. 3)
395   During 2015-2016, we just started using UAVs to monitor the health of the grassland, and the suitable camera parameters
and methods were still under exploration. Therefore, many photos with abnormal white balance reduced the accuracy of
AGB estimation at the photo scale (Figure 12). 4) We only collected grassland AGB in the peak season of vegetation growth,
and whether the proposed method applies to other growing seasons remains to be further investigated. 5) During the
modeling process, the center points of the flight route were used to find the matching MODIS pixels due to the limited
400   positioning accuracy. Moreover, although the UAV images from GRID or RECTANGLE mode could cover most areas of a
MODIS pixel, full pixel coverage was still not achieved. Therefore, we will gradually scale up to MODIS pixels by
combining UAVs with Sentinel-2 or Landsat images.

5. Data availability

The dataset is available from the National Tibetan Plateau/Third Pole Environment Data Center at
405   https://doi.org/10.11888/Terre.tpdc.272587. The dataset contains 20 years of AGB spatial data of the QTP with a resolution
of 250 m and is stored in TIFF format. The name of the file is "AGB_yyyy.tif", where yyyy represents the year. For example,
AGB_2000.tif represents this TIFF file describing the alpine grassland AGB condition of QTP in 2005. The data can be
readily imported into standard geographical information system software (e.g., ArcGIS) or accessed programmatically (e.g.,
MATLAB, Python).

410   **6. Conclusion**

This study presents a new gridded dataset of alpine grassland AGB over the QTP based on traditional ground sampling,
UAV photographing, and MODIS images. The uniqueness of this dataset is that when obtaining ground verification data, the
UAV is used as a scale matching bridge between traditional local measurement samples and satellite pixels. The study
confirmed that the UAV images could be used for AGB estimation at the quadrat /pixel scale, with R^2 of 0.73/0.83 and
415   RMSE of 44.23/34.13 g/m^2, respectively. At the pixel scale, the AGB estimated by UAV was more correlated with the
MODIS vegetation indices than the traditional ground sampling method (0.88 VS 0.53), and the scale matching of the
dependent and the independent variables was achieved during model construction. In addition, the constructed pixel scale

model has been independently cross-validated over many years (2015-2019), which confirmed the robustness of the model and ensured the accuracy of this dataset. Availability of the new dataset is helpful in many applications. First, this dataset

420 provides reliable regional data for estimating grassland productivity, carbon storage, ecological environment carrying capacity, and ecological service functions (such as feed for grazing livestock) on the QTP. Second, the dataset can be used to understand the mechanisms of environmental processes, such as hydrological cycle processes, soil erosion and degradation, and carbon cycle processes in the QTP. In addition, this dataset can be used as input or validation parameters for various ecological models to understand the response mechanism of the QTP to global climate change.

425 **7. Author contributions**

HZ contributed to the study conceptualization, methodology, funding acquisition, and the original draft of the manuscript. ZT, BW and HK contributed to resources and formal analysis. QY and YS contributed to data collection and manuscript review. BM, ML, and JC contributed to the methodology and reviewed the manuscript. YL and JZ participated in reviewing and editing the manuscript. SN contributed to the data collection and review of the manuscript. SY contributed to the study

430 conceptualization, funding acquisition, and manuscript review. All authorship have read and approved the manuscript.

8. Competing interests

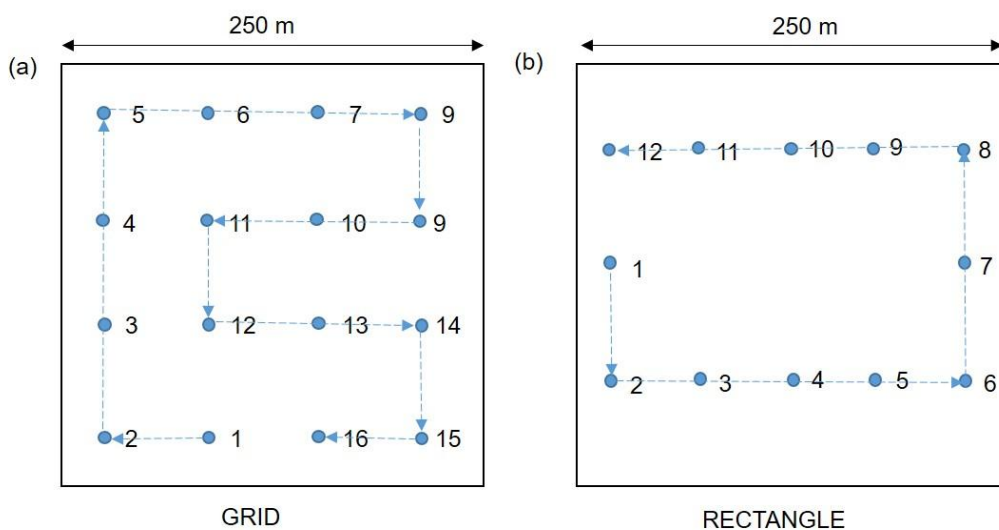The authors declare that they have no conflict of interest.

9. Acknowledgements

435 **10. Financial support**

Appendix

440

Figure A1. Waypoints for GRID (a) and RECTANGLE (b) flight modes.
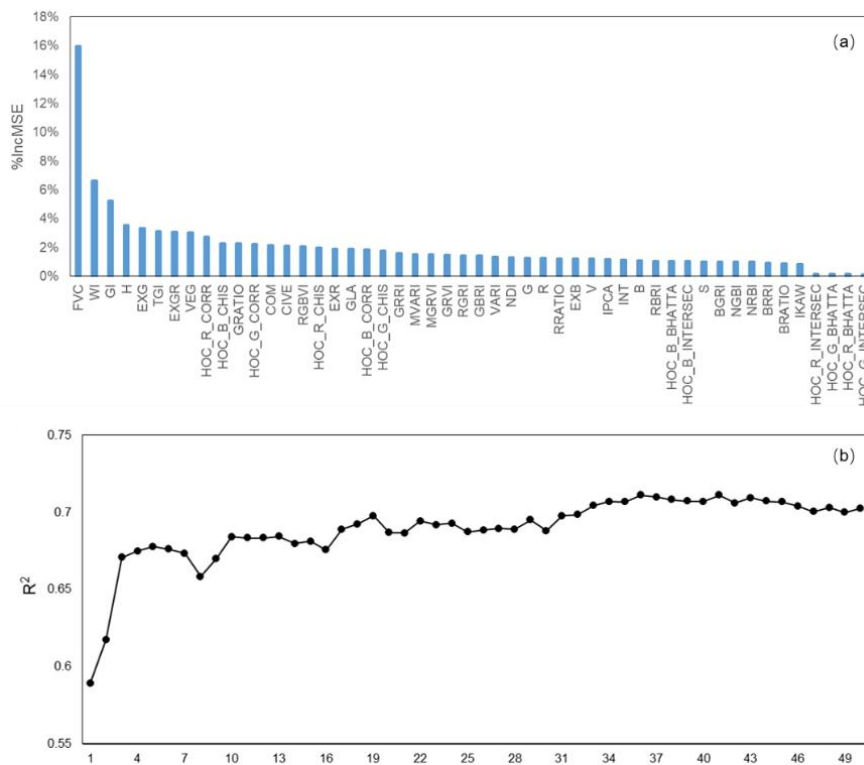

Figure A2. The importance value for each independent variable (a) and the R^2 results of the different number of input variables at the quadrat scale.

Earth System
Science
Data
Open Access
Discussions

445
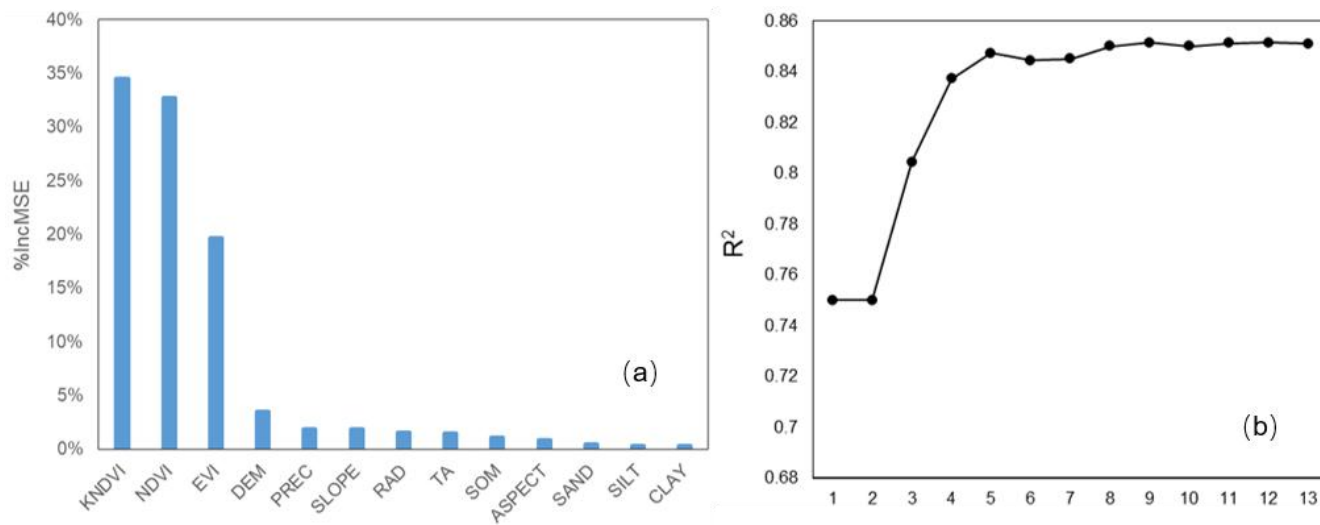
Figure A3. The importance value for each independent variable (a) and the R^2 results of the different number of input variables at the pixel scale.

450

Table A1. Features of DJI Phantom 3 Pro

	Features	Description
	Sensor	1/23-inch; Effective-pixel: 12-megapixel
	Filed of view	FOV 94° 20 mm
	Aperture	f/2.8
	Shooting speed	Electronic shutter: 8-1/8000 s
	Photo size	4000×3000
	Flight time	~25 min
DJI Phantom 3 Pro	Image format	JPEG
	Hovering accuracy	±0.5 m vertically; ±1.5 m horizontally
	Weight	1280 g

455

Table A2: Details of the independent variables for quadrat-scale AGB estimation

Acronym	Index name	Formula	Reference
GRVI	Green Red Vegetation Index	$(G-R)/(G+R)$	(Tucker, 1979)
EXG	Excess Green Vegetation Index	$2G-R-B$	(Woebbecke et al., 1995)
GLA	Green leaf area	$(2G-R-B)/(2G+R+B)$	(Louhaichi et al.)
MGRVI	Modified Green Blue Vegetation Index	$(G2-R2)/(G2+R2)$	(Bendig et al., 2015)
RGBVI	Red Green Blue Vegetation Index	$(G2-B*R)/(G2+B*R)$	(Bendig et al., 2015)
EXB	Excess Blue Vegetation Index	$(1.4*B-G)/(G+R+B)$	(Maimaitijiang et al., 2019)
NDI	Normalized difference index	$(R-G)/(R+G)$	(Woebbecke et al., 1993)
EXR	Excess Red Vegetation Index	$1.4*R-B$	(Meyer and Neto, 2008)
EXGR	Excess Green minus Excess Red index	$ExG-ExR$	(Meyer and Neto, 2008)
RRATIO	Red Ratio	$R/(R+B+G)$	(Woebbecke et al., 1995)
BRATIO	Blue Ratio	$B/(R+B+G)$	(Woebbecke et al., 1995)
GRATIO	Green Ratio	$G/(R+B+G)$	(Woebbecke et al., 1995)
VARI	Visible Atmospherically Resistance Index	$(G-R)/(G+R-B)$	(Gitelson et al., 2002)
NRBI	Normalized Red Blue Index	$(R-B)/(R+B)$	(Michez et al., 2016)
NGBI	Normalized Green Blue Index	$(G-B)/(G+B)$	(Michez et al., 2016)
VEG	Vegetative index	$G/(R^a B^{(1-a)})$, where $a=0.667$	(Hague et al., 2006)
WI	Woebbecke Index	$(G-B)/(R-G)$	(Woebbecke et al., 1995)
CIVE	Color Index of Vegetation	$0.441R - 0.881G+0.385B+18.78745$	(Kataoka et al., 2003)
COM	Combination Vegetative index	$0.25ExG+0.3ExGR+0.33CIVE +0.12VEG$	(Guijarro et al., 2011)
TGI	Triangular Greenness Index	$G-0.39R-0.61B$	(Hunt et al., 2014; Michez et al., 2018)
RGBVI	Red Green Blue Vegetation Index	$(G2-B*R)/(G2+B*R)$	(Bendig et al., 2015)
GRRI	Green Red Ratio Index	G/R	(Maimaitijiang et al., 2019)
GBRI	Green Blue Ratio Index	G/B	(Maimaitijiang et al., 2019)
RBRI	Red Blue Ratio Index	R/B	(Maimaitijiang et al., 2019)
BRRI	Blue Red Ratio Index	B/R	(Jibo et al., 2018)
BGRI	Blue Green Ratio Index	B/G	(Jibo et al., 2018)
RGRI	Red Green Ratio Index	R/G	(Jibo et al., 2018)
INT	Color Intensity Index	$(R+B+G)/3$	(Ahmad and Reid, 1996)
MVARI	Modified VARI	$(G-B)/(G+R-B)$	(Cen et al., 2019)
IPCA	Principal Component Analysis Index	$0.994\times|R-B|+ 0.961\times|G-B|+ 0.914\times|G-R|$	(Saberioon et al., 2014)

460

Table A2: Details of the independent variables for quadrat-scale AGB estimation（continued）

Acronym	Index name	Formula	Reference
R	An average value of R channel of the quadrat-scale UAV image		
G	An average value of G channel of the quadrat-scale UAV image		
B	An average value of B channel of the quadrat-scale UAV image		
H	An average value of H channel of the quadrat-scale image in HSV color space		
S	An average value of S channel of the quadrat-scale image in HSV color space		
V	An average value of V channel of the quadrat-scale image in HSV color space		
FVC	Fractional Vegetion Cover		
EGI	Extra Geen Index	EGI=2G-R-B	(Zhang et al., 2022)
GI	Green Index	GI=9×(H×3.14159/180) +3×S+V	
HOC_i_CORR	The histogram correlation coefficient between the i band and the black reference histogram, where the i represents the three bands of RGB	$corr \dfrac{\sum_I (H_1(I) - \bar{H}_1)(H_2(I) - \bar{H}_2)}{\sqrt{\sum_I (H_1(I) - \bar{H}_1)^2 \sum_I (H_2(I) - \bar{H}_2)^2}}$	
HOC_i_INTERSEC	The histogram intersection coefficient between the i band and the black reference histogram, where the i represents the three bands of RGB	$intersec = \sum_I \min (H_1(I), H_2(I))$	
HOC_i_BHATTA	The histogram Bhattacharyya distance coefficient between the i band and the black reference histogram, where the i represents the three bands of RGB	$bhatta = \sum_I \min (H_1(I), H_2(I))$	
HOC_i_CHIS	The histogram correlation coefficient between the i band and the black reference histogram, where the i represents the three bands of RGB.	$chis = \sum_I \dfrac{\left(H_1(I) - H_2(I)\right)^2}{H_1(I)}$	

Earth System
Science
Data
Open Access
Discussions

References

Ahmad, I. S. and Reid, J. F.: Evaluation of Colour Representations for Maize Images, Journal of Agricultural Engineering Research, 63,
465   185-195, doi:10.1006/jaer.1996.0020 1996.4

Bendig, J., Yu, K., Aasen, H., Bolten, A., Bennertz, S., Broscheit, J., Gnyp, M. L., and Bareth, G.: Combining UAV-based plant height from crop surface models, visible, and near infrared vegetation indices for biomass monitoring in barley, International Journal of Applied Earth Observation & Geoinformation, 39, 79-87, doi:10.1016/j.jag.2015.02.012, 2015.4

Bian, L. and Walsh, S. J.: Scale dependencies of vegetation and topography in a mountainous environment of Montana, The Professional
470   Geographer, 45, 1-11, doi:10.1111/j.0033-0124.1993.00001.x, 1993.4

Breiman, L.: Random forests, Machine learning, 45, 5-32, doi:10.1023/A:1010933404324, 2001.4

Camps-Valls, G., Campos-Taberner, M., Moreno-Martinez, A., Walther, S., Duveiller, G., Cescatti, A., Mahecha, M. D., Munoz-Mari, J., Garcia-Haro, F. J., Guanter, L., Jung, M., Gamon, J. A., Reichstein, M., and Running, S. W.: A unified vegetation index for quantifying the terrestrial biosphere, Sci Adv, 7, eabc7447, doi:10.1126/sciadv.abc7447, 2021.4

475   Cannavacciuolo, M., Bellido, A., Cluzeau, D., Gascuel, C., and Trehen, P.: A geostatistical approach to the study of earthworm distribution in grassland, Applied Soil Ecology, 9, 345-349, doi:10.1016/S0929-1393(98)00087-0, 1998.4

Cen, H. Y., Wan, L., Zhu, J. P., Li, Y. J., Li, X. R., Zhu, Y. M., Weng, H. Y., Wu, W. K., Yin, W. X., Xu, C., Bao, Y. D., Feng, L., Shou, J. Y., and He, Y.: Dynamic monitoring of biomass of rice under different nitrogen treatments using a lightweight UAV with dual image-frame snapshot cameras, Plant Methods, 15, doi:10.1186/s13007-019-0418-8, 2019.4

480   Chen, J., Yi, S., Qin, Y., and Wang, X.: Improving estimates of fractional vegetation cover based on UAV in alpine grassland on the Qinghai–Tibetan Plateau, International Journal of Remote Sensing, 37, 1922-1936, doi:10.1080/01431161.2016.1165884, 2016.4

Cheng, X., An, S., Chen, J., Li, B., Liu, Y., and Liu, S.: Spatial relationships among species, above-ground biomass, N, and P in degraded grasslands in Ordos Plateau, northwestern China, Journal of Arid Environments, 68, 652-667, doi:10.1016/j.jaridenv.2006.07.006, 2007.4

Crow, W. T., Berg, A. A., Cosh, M. H., Loew, A., Mohanty, B. P., Panciera, R., de Rosnay, P., Ryu, D., and Walker, J. P.: Upscaling
485   sparse ground‐based soil moisture observations for the validation of coarse‐resolution satellite soil moisture products, Reviews of Geophysics, 50, doi:10.1029/2011rg000372, 2012.4

Dancy, K., Webster, R., and Abel, N.: Estimating and mapping grass cover and biomass from low-level photographic sampling, International Journal of Remote Sensing, 7, 1679-1704, doi:10.1080/01431168608948961, 1986.4

Ding, M. J., Zhang, Y. L., Sun, X. M., Liu, L. S., Wang, Z. F., and Bai, W. Q.: Spatiotemporal variation in alpine grassland phenology in
490   the Qinghai-Tibetan Plateau from 1999 to 2009, Chinese Science Bulletin, 58, 396-405, doi:10.1007/s11434-012-5407-5, 2013.4

Dusseux, P., Hubert-Moy, L., Corpetti, T., and Vertes, F.: Evaluation of SPOT imagery for the estimation of grassland biomass, International Journal of Applied Earth Observation and Geoinformation, 38, 72-77, doi:10.1016/j.jag.2014.12.003, 2015.4

Gao, X. X., Dong, S. K., Li, S., Xu, Y. D., Liu, S. L., Zhao, H. D., Yeomans, J., Li, Y., Shen, H., Wu, S. N., and Zhi, Y. L.: Using the random forest model and validated MODIS with the field spectrometer measurement promote the accuracy of estimating aboveground
495   biomass and coverage of alpine grasslands on the Qinghai-Tibetan Plateau, Ecological Indicators, 112, 106114, doi:10.1016/j.ecolind.2020.106114, 2020.4

Ghosh, S. M. and Behera, M. D.: Aboveground biomass estimation using multi-sensor data synergy and machine learning algorithms in a dense tropical forest, Applied Geography, 96, 29-40, doi:10.1016/j.apgeog.2018.05.011, 2018.4

Gitelson, A. A., Kaufman, Y. J., Stark, R., and Rundquist, D.: Novel algorithms for remote estimation of vegetation fraction, Remote
500   Sensing of Environment, 80, 76-87, doi:10.1016/s0034-4257(01)00289-9 2002.4

Guijarro, M., Pajares, G., Riomoros, I., Herrera, P. J., Burgos-Artizzu, X. P., and Ribeiro, A.: Automatic segmentation of relevant textures in agricultural images, Computers & Electronics in Agriculture, 75, 75-83, doi:10.1016/j.compag.2010.09.013, 2011.4

Hague, T., Tillett, N. D., and Wheeler, H.: Automated Crop and Weed Monitoring in Widely Spaced Cereals, Precision Agriculture, 7, 21-32, doi:10.1007/s11119-005-6787-1, 2006.4

505   He, L., Li, A. N., Yin, G. F., Nan, X., and Bian, J. H.: Retrieval of Grassland Aboveground Biomass through Inversion of the PROSAIL Model with MODIS Imagery, Remote Sensing, 11, 1597, doi:10.3390/rs11131597, 2019.4

Hunt, E. R., Daughtry, C. S. T., Mirsky, S. B., and Hively, W. D.: Remote Sensing With Simulated Unmanned Aircraft Imagery for Precision Agriculture Applications, IEEE Journal of Selected Topics in Applied Earth Observations & Remote Sensing, 7, 4566-4571, doi:doi:10.1109/jstars.2014.2317876, 2014.4

510   Jia, W., Liu, M., Yang, Y., He, H., Zhu, X., Yang, F., Yin, C., and Xiang, W.: Estimation and uncertainty analyses of grassland biomass in Northern China: Comparison of multiple remote sensing data sources and modeling approaches, Ecological indicators, 60, 1031-1040, doi:10.1016/j.ecolind.2015.09.001, 2016.4

Jiao, C., Yu, G., He, N., Ma, A., and Hu, Z.: The spatial pattern of grassland aboveground biomass and its environmental controls in the Eurasian steppe, doi:10.11821/dlxb201605007, 2016.4

515   Jibo, Y., Haikuan, F., Xiuliang, J., Huanhuan, Y., Zhenhai, L., Chengquan, Z., Guijun, Y., and Qingjiu, T.: A Comparison of Crop Parameters Estimation Using Images from UAV-Mounted Snapshot Hyperspectral Sensor and High-Definition Digital Camera, Remote Sensing, 10, 1138-, doi:10.3390/rs10071138, 2018.4

Kataoka, T., Kaneko, T., Okamoto, H., and Hata, S.: Crop growth estimation system using machine vision, Advanced Intelligent Mechatronics, 2003. AIM 2003. Proceedings. 2003 IEEE/ASME International Conference on, Crop growth estimation system using machine vision,

Kohavi, R.: A study of cross-validation and bootstrap for accuracy estimation and model selection, Ijcai, 1137-1145, doi:10.1109/jstars.2014.2317876,

Li, M., Wu, J., Feng, Y., Niu, B., He, Y., and Zhang, X.: Climate variability rather than livestock grazing dominates changes in alpine grassland productivity across Tibet, Frontiers in Ecology and Evolution, 9, doi:10.3389/fevo.2021.631024, 2021.4

Li, X., Liu, S., Li, H., Ma, Y., Wang, J., Zhang, Y., Xu, Z., Xu, T., Song, L., and Yang, X.: Intercomparison of six upscaling evapotranspiration methods: From site to the satellite pixel, Journal of Geophysical Research: Atmospheres, 123, 6777-6803, doi:10.1029/2018jd028422, 2018.4

Liu, S., Cheng, F., Dong, S., Zhao, H., Hou, X., and Wu, X.: Spatiotemporal dynamics of grassland aboveground biomass on the Qinghai-Tibet Plateau based on validated MODIS NDVI, Scientific reports, 7, 1-10, doi:10.1038/s41598-017-04038-4, 2017.4

Louhaichi, M., Borman, M. M., and Johnson, D.: Spatially Located Platform and Aerial Photography for Documentation of Grazing Impacts on Wheat, Geocarto International, doi:10.1080/10106040108542184,

Lussem, U., Bolten, A., Menne, J., Gnyp, M. L., Schellberg, J., and Bareth, G.: Estimating biomass in temperate grassland with high resolution canopy surface models from UAV-based RGB images and vegetation indices, Journal of Applied Remote Sensing, 13, 034525, doi:10.1117/1.Jrs.13.034525, 2019.4

Maimaitijiang, M., Sagan, V., Sidike, P., Maimaitiyiming, M., Hartling, S., Peterson, K. T., Maw, M. J. W., Shakoor, N., Mockler, T., and Fritschi, F. B.: Vegetation Index Weighted Canopy Volume Model (CVM VI) for soybean biomass estimation from Unmanned Aerial System-based RGB imagery, ISPRS Journal of Photogrammetry and Remote Sensing, 151, 27-41, doi:10.1016/j.isprsjprs.2019.03.003, 2019.4

Meng, B., Yi, S., Liang, T., Yin, J., and Sun, Y.: Modeling alpine grassland above ground biomass based on remote sensing data and machine learning algorithm: A case study in the east of Tibetan Plateau, China, IEEE Journal of Selected Topics in Applied Earth Observations and Remote Sensing, PP, 1-1, doi:10.1109/Jstars.2020.2999348, 2020.4

Meyer, G. E. and Neto, J. C.: Verification of color vegetation indices for automated crop imaging applications, Computers and Electronics in Agriculture, 63, 282-293, doi:10.1016/j.compag.2008.03.009, 2008.4

Michez, A., Piégay, H., Lisein, J., Claessens, H., and Lejeune, P.: Classification of riparian forest species and health condition using multi-temporal and hyperspatial imagery from unmanned aerial system, Environmental Monitoring & Assessment, 188, 1-19, doi:10.1007/s10661-015-4996-2, 2016.4

Michez, A., Bauwens, S., Brostaux, Y., Hiel, M. P., Garré, S., Lejeune, P., and Dumont, B.: How Far Can Consumer-Grade UAV RGB Imagery Describe Crop Production? A 3D and Multitemporal Modeling Approach Applied to Zea mays, Remote Sensing, 10, doi:10.3390/rs10111798, 2018.4

Morais, T. G., Teixeira, R. F., Figueiredo, M., and Domingos, T.: The use of machine learning methods to estimate aboveground biomass of grasslands: A review, Ecological Indicators, 130, 108081, doi:10.1016/j.ecolind.2021.108081, 2021.4

Mutanga, O., Adam, E., and Cho, M. A.: High density biomass estimation for wetland vegetation using WorldView-2 imagery and random forest regression algorithm, International Journal of Applied Earth Observation and Geoinformation, 18, 399-406, doi:10.1016/j.jag.2012.03.012, 2012.4

O'Mara, F. P.: The role of grasslands in food security and climate change, Annals of botany, 110, 1263-1270, doi:10.1093/aob/mcs209, 2012.4

Ramankutty, N., Evan, A. T., Monfreda, C., and Foley, J. A.: Farming the planet: 1. Geographic distribution of global agricultural lands in the year 2000, Global biogeochemical cycles, 22, doi:10.1029/2007GB002952, 2008.4

Saberioon, M. M., Amin, M., Anuar, A. R., Gholizadeh, A., Wayayok, A., and Khairunniza-Bejo, S.: Assessment of rice leaf chlorophyll content using visible bands at different growth stages at both the leaf and canopy scale, International Journal of Applied Earth Observations & Geoinformation, 32, 35-45, doi:10.1016/j.jag.2014.03.018, 2014.4

Suttie, J. M., Reynolds, S. G., and Batello, C.: Grasslands of the World, Food & Agriculture Org.2005.

Tucker, C. J.: Red and photographic infrared linear combinations for monitoring vegetation, Remote Sensing and Environment, 8, 127-150, doi:10.1016/0034-4257(79)90013-0, 1979.4

Vergara, J. R. and Estévez, P. A.: A review of feature selection methods based on mutual information, Neural computing and applications, 24, 175-186, doi:10.1007/s00521-013-1368-0, 2014.4

Viljanen, N., Honkavaara, E., Näsi, R., Hakala, T., Niemeläinen, O., and Kaivosoja, J.: A novel machine learning method for estimating biomass of grass swards using a photogrammetric canopy height model, images and vegetation indices captured by a drone, Agriculture, 8, 70, doi:10.3390/agriculture8050070, 2018.4

Wang, J. and Sun, W.: Multiscale geostatistical analysis of sampled above-ground biomass and vegetation index products from HJ-1A/B, Landsat, and MODIS, Land Surface Remote Sensing II, 92601T, 10.1117/12.2069008,

Wang, J., Ge, Y., Song, Y., and Li, X.: A geostatistical approach to upscale soil moisture with unequal precision observations, IEEE Geoscience and Remote Sensing Letters, 11, 2125-2129, doi:10.1109/Lgrs.2014.2321429, 2014.4

575 Wang, J., Xiao, X., Bajgain, R., Starks, P., Steiner, J., Doughty, R. B., and Chang, Q.: Estimating leaf area index and aboveground biomass of grazing pastures using Sentinel-1, Sentinel-2 and Landsat images, ISPRS Journal of Photogrammetry and Remote Sensing, 154, 189-201, doi:10.1016/j.isprsjprs.2019.06.007, 2019.4

Wang, L. a., Zhou, X., Zhu, X., Dong, Z., and Guo, W.: Estimation of biomass in wheat using random forest regression algorithm and remote sensing data, The Crop Journal, 4, 212-219, doi:10.1016/j.cj.2016.01.008, 2016.4

Wang, Y., Wu, G., Deng, L., Tang, Z., Wang, K., Sun, W., and Shangguan, Z.: Prediction of aboveground grassland biomass on the Loess
580 Plateau, China, using a random forest algorithm, Scientific reports, 7, 1-10, doi:10.1038/s41598-017-07197-6, 2017.4

Woebbecke, D. M., Meyer, G. E., Bargen, K. V., and Mortensen, D. A.: Color Indices for Weed Identification Under Various Soil, Residue, and Lighting Conditions, Transactions of the Asae, 38, 259-269, doi:10.1109/jstars.2014.2317876 1995.4

Woebbecke, D. M., Meyer, G. E., Von Bargen, K., and Mortensen, D. A.: Plant species identification, size, and enumeration using machine vision techniques on near-binary images, Optics in Agriculture and Forestry, 208-219, 10.1117/12.144030

585 Xia, J., Ma, M., Liang, T., Wu, C., Yang, Y., Zhang, L., Zhang, Y., and Yuan, W.: Estimates of grassland biomass and turnover time on the Tibetan Plateau, Environmental Research Letters, 13, 014020, doi:10.1088/1748-9326/aa9997, 2018.4

Yang, S., Feng, Q., Liang, T., Liu, B., Zhang, W., and Xie, H.: Modeling grassland above-ground biomass based on artificial neural network and remote sensing in the Three-River Headwaters Region, Remote Sensing of Environment, S0034425717304741, doi:10.1016/j.rse.2017.10.011, 2017.4

590 Yang, Y., Fang, J., Pan, Y., and Ji, C.: Aboveground biomass in Tibetan grasslands, Journal of Arid Environments, 73, 91-95, doi:10.1016/j.jaridenv.2008.09.027, 2009.4

Yang, Y., Fang, J., Ma, W., Guo, D., and Mohammat, A.: Large‐scale pattern of biomass partitioning across China's grasslands, Global Ecology and Biogeography, 19, 268-277, doi:10.1111/j.1466-8238.2009.00502.x, 2010.4

Yi, S.: FragMAP: a tool for long-term and cooperative monitoring and analysis of small-scale habitat fragmentation using an unmanned
595 aerial vehicle, International Journal of Remote Sensing, 38, 2686-2697, doi:10.1080/01431161.2016.1253898, 2017.4

Yu, R., Yao, Y., Wang, Q., Wan, H., Xie, Z., Tang, W., Zhang, Z., Yang, J., Shang, K., and Guo, X.: Satellite-Derived Estimation of Grassland Aboveground Biomass in the Three-River Headwaters Region of China during 1982–2018, Remote Sensing, 13, 2993, doi:10.3390/rs13152993, 2021.4

Zeng, N., Ren, X., He, H., Zhang, L., Zhao, D., Ge, R., Li, P., and Niu, Z.: Estimating grassland aboveground biomass on the Tibetan
600 Plateau using a random forest algorithm, Ecological Indicators, 102, 479-487, doi:10.1016/j.ecolind.2019.02.023, 2019.4

Zhang, B., Zhang, L., Xie, D., Yin, X., Liu, C., and Liu, G.: Application of synthetic NDVI time series blended from Landsat and MODIS data for grassland biomass estimation, Remote Sensing, 8, 10, doi:10.3390/rs8010010, 2016.4

Zhang, H., Sun, Y., Chang, L., Qin, Y., Chen, J., Qin, Y., Du, J., Yi, S., and Wang, Y.: Estimation of grassland canopy height and aboveground biomass at the quadrat scale using unmanned aerial vehicle, Remote sensing, 10, 851, doi:10.3390/rs10060851, 2018.4

605 Zhang, H. F., Tang, Z. G., Wang, B. Y., Meng, B. P., Qin, Y., Sun, Y., Lv, Y. Y., Zhang, J. G., and Yi, S. H.: A non-destructive method for rapid acquisition of grassland aboveground biomass for satellite ground verification using UAV RGB images, Global Ecology and Conservation, 33, e01999, doi:10.1016/j.gecco.2022.e01999, 2022.4